



## Ab-initio Assessment of the Electronic, Mechanical, Thermal, Optical and Phonon Properties of B3-AIAs

E. E. Gregory, S. A. Ekong\*, J. B. Emah

Received: February 17, 2024 / Accepted: April 20, 2024  
© REJOST 2024

### Abstract

The applications of group III–V minerals are closely linked to their structural and compositional polymorphs and have drawn great attention due to their vast electronic and optoelectronic technology. Aluminum arsenide (AIAs) is a group III–V coordinated tetrahedral crystal material. The present investigation addresses the aspects of optical extinction coefficient, energy loss function, refractive index, and reflectivity of the B3-phase AIAs which are still missing in reported studies. Optical properties can be used to show materials application to birefringent. This work aims at giving a deep understanding of B3-phase AIAs minerals, in terms of electronic structure, bond strength, mechanical properties, dynamical and optical properties. In this paper, ab-initio assessment of the above properties is carried out using the methods of density functional theory (DFT) as implemented in quantum espresso and thermo\_pw codes. The material simulations are performed self-consistently by using pseudopotentials in the form of generalized gradient approximation (GGA) and local density approximation (LDA) respectively, to account for the exchange correlations. The energy and charge density convergence tests were examined to study the ground-state properties. The band structure and density of state (DOS) diagrams plotted demonstrate an indirect semiconducting state with an energy band gap of 1.45 eV (GGA) and 1.34 eV (LDA), as well as Al-As bond length, all in satisfactory accord with data from experiment and theory. Mechanically, analysis of the 3D-projections demonstrates that B3-AIAs possesses a high degree of anisotropy, which is further confirmed by the calculated Zener- and universal-anisotropic indexes. The evaluated Debye temperature  $\theta_{(D)} = 397.724$  K reflects the feasibility of the material being brittle, while the Debye heat capacity  $C_V = 49.63 J/(K.mol)$  reveals the Dulong-Petit limit. The Debye frequency ( $\omega_D$ ) and Grüneisen's parameter ( $\gamma$ ) calculated are depicted for the first time. The general profiles of the optically dependent dielectric functions of B3-AIAs under ambient conditions are discussed. Analysis of the obtained

optical parameters, such as the reflectivity, refractive index, extinction coefficient, and energy loss function suggests the material is a good dielectric due to the appearance of the spectrum mostly in the ultra-violet region.

✉ Sylvester. A. Ekong: [sylvesterekong@aksu.edu.ng](mailto:sylvesterekong@aksu.edu.ng)

Department of Physics, Akwa Ibom State University, Ikot Akpaden, P.M.B. 1167, Uyo, Nigeria

**Keywords:** Electronic structure, Elastic constant, Mechanical properties, Phonon dispersion and Optical properties.

## 1.0 Introduction

The operational characteristics of materials are not only very crucial at practical device levels for electronic and opto-electronic engineering technology but are also associated with and needed for a better understanding of the material's properties behind the fundamental science. The continual and increasing interest in the behavior of semiconducting devices at varying conditions is remarkable, and has been applauded for the vast number of high-quality calculations performed on group II–VI, III–V, and IV materials (Mujica *et al.*, 2003; Srivastava *et al.*, 2011; Xing-xiu *et al.*, 2013; Lebga *et al.*, 2018). Primarily, of these groups, the driving force behind group III–V materials studies is of immense technological importance, owing to their applications in the fabrication of fast microelectronic devices. Consequently, such compounds play a vital role in areas of high frequency devices with low noise, such as mobile telephones, material advancements in spintronics, the design of light emitting diodes, etc. (Srivastava *et al.*, 2011, with references therein). Considerable attention has over the years been drawn to the study of the structural and electronic properties of complex systems, where the focus from both theoretical reports and experiments has been on understanding the related properties of a variety of compound semiconductors (Mujica *et al.*, 2003; Gupta and Kulshrestha, 2009; Greene *et al.*, 1994). Intriguingly, tetrahedrally

coordinated structures are most remarkable for exhibiting low density and can undergo transformation when pressure-driven into higher density structures. The attribute of the homopolar members of this semiconductor is the meager ratio of the volume of touching atom spheres to the unit-cell of 0.34 compared to the close-packed elemental structure ratio (0.74) (Srivastava *et al.*, 2011).

Aluminum arsenide (AlAs) being a coordinated tetrahedral material in group III–V semiconductors, has attracted large interest owing to its candidacy as a promising pure optoelectronic material at room temperature. AlAs crystallizes in the zinc-blende (B3) inverse spinel structures at normal conditions and detailed studies of the energetics have been reported (Jappor *et al.*, 2013; Mujica *et al.*, 2003; Xing-xiu *et al.*, 2013). The excellent physical properties exhibited make it attractive for better device applications. For instance, the stimulated technology in the formation of epitaxial multilayer structures with gallium arsenide (GaAs) is well applauded alongside its use in heterojunction bipolar transistors, photodetectors, tunable devices for visible wavelength, electro-optic modulators, high electronic mobility transistors, solid state lasers, frequency-mixing components, etc. (Li *et al.*, 2012; Kimukin *et al.*, 2004; Liu *et al.*, 1994; Vurgaftman *et al.*, 2001). Experimentally, Greene and coworkers measured and reported the lattice constant (5.66 Å) for the

four -fold coordinated zinc-blende (B3) structure at ambient conditions (Greene *et al.*, 1994).

Ab-initio electronic structure computation as a fundamental first-principle method employs the formalism of density functional theory (DFT) (Hohenberg and Sham, 1965). This has been of great importance to several material studies in areas not limited to energy storage devices, photonics, optoelectronics, nanoscience, earth-physics, photochemistry and thermoelectricity (Shafei *et al.*, 2021; Ekong *et al.*, 2014; Bashi *et al.*, 2021; Jolayemi *et al.*, 2020; Ekong *et al.*, 2015; Lavrentyev *et al.*, 2017; Jolayemi *et al.*, 2019). Earlier ab-initio pseudopotential research tremendously worked on the structural stability of AlAs polymorphs, and found the zinc-blende (B3) phase to be thermodynamically most stable (Varshney *et al.*, 2009; Mujica *et al.*, 1999; 2003; 1995; Zhang *et al.*, 1987; Froyen *et al.*, 1983).

Nevertheless, other properties of zinc-blende (B3) AlAs have been investigated by other researchers. In this light, Jappor *et al.*, using ab-initio self-consistent Hartree-Fock scheme, reported a molecular orbital study of zinc-blende AlAs based on electronic structure nanocrystals (Jappor *et al.*, 2013). Previous characterization by Mujica *et al.* (1995), performed first-principles pseudopotential study of the zinc-blende, wurtzite, sodium chloride (NaCl), cesium chloride (CsCl),  $\beta$ -tin, nickel arsenide (NiAs), and simple cubic (sc)-16 structural phases, and reported the phase stability of GaAs and AlAs semiconductors. Gupta *et al.* (2009), calculated the ground state properties of B3-AlAs structure based on ab-initio pseudopotential method within the DFT formalism. They employed the local density approximation (LDA) for the exchange - correlation energy parameterization. Their reports revealed that the valence band maximum (VBM) and conduction band minimum (CBM) occurred at the  $\Gamma \rightarrow X$  symmetry points, thus depicting an indirect

energy gap value of 1.33eV, compared to the experiment (2.15eV). Further investigations by Jiang *et al.* (2018) reported a first-principles study of point defects in GaAs/AlAs superlattice. According to them, the effects on the band structure and carrier mobility results advances the understanding of the radiation damage effects of GaAs/AlAs semiconductor superlattice based electronic and optoelectronics, for extreme environmental applications (Jiang *et al.*, 2018). Earlier DFT calculations by Li *et al.* (2012), reported on the lattice dynamic properties of XAs (X =Al, Ga and In) with zinc-blende (B3) structure from first-principle. They recorded a lattice constant of 5.64Å for the bulk B3-AlAs structure within a GGA. Also, in their discussions of the band structure, density of state and vibrational properties, only the static dielectrics were accounted for (Li *et al.*, 2012), thus leaving a gap for further study. Recently, Tandon *et al.* (2018) in a first principles calculation to predict the electron-phonon (e-ph) scattering rates in B3-AlAs, studied the dependence of phonon modes at energies close to the conduction minima. They reported an energy band-gap of 1.35eV at  $\Gamma \rightarrow X$  symmetry along with effects of phonon dispersion shift from the optical phonon bands to higher frequencies, as well as in acoustic branches to lower frequencies.

In light of the above, to the best of our knowledge, optical parameters such as the extinction coefficient, refractive index, reflectivity, energy loss function and related thermal properties like the Debye frequency ( $\omega_D$ ) and Grüneisen's parameter of bulk B3-phase AlAs have not yet been explore and are still lacking in the literature, thus necessitating this study. Also, apart from the static dielectric constant accounted for by Li *et al.* (2012), there is no other optical reports on bulk B3-AlAs so far. This paper provides a one-stop shop for the fundamental understanding of B3-AlAs structure

owing to a comprehensive study of the electronic, elastic, mechanical, thermal, optical and phonon dynamical properties of the material, which apparently is the aim of this paper. The high anisotropy displayed in this paper is further confirmed by the obtained elastic-matrix shown using 2D-projections and 3D representations.

## 2.0 Computational Procedure

The first-principles calculations describing the ground-state properties of AlAs have been performed based on DFT using plane-wave expansion of wave function as implemented in Quantum Espresso code (Giannozzi *et al.*, 2009). By employing the generalized gradient approximation (GGA) with Perdew-Burke-Ernzerhof (PBE) functional (Perdew *et al.* 1996), the exchange-correlation energy was determined. Force interactions for linear responses between the electron-ion, ion-ion, and electron-electron of the Al and As atoms are elucidated by norm-conserving gaussian-type pseudopotentials within the local density approximation (LDA) (Goedecker and Teter 1996, Hartwigsen *et al.*, 1998). The expanded electromagnetic wave functions required a plane wave basis set with kinetic energy cut-off of 180 Ry (for GGA) and 150 Ry (for LDA) respectively. The pseudo potentials depict the ionic cores for Al and As atoms, where the configurations: Al –  $3s^23p^1$  electrons, and As –  $4s^24p^3$  electrons are explicitly treated as valence electrons. By employing the Monkhorst-Pack scheme (Monkhorst and Pack, 1976), a Brillouin zone (BZ) sampling with  $8 \times 8 \times 8$  and  $10 \times 10 \times 10$  grids was used in the primitive-cell geometry of AlAs. The optimization of the geometry is favored by the chosen cut-off energy and BZ sampling k-point grids as assured by the convergence criteria for ionic minimization given as  $2.0 \times 10^{-6}$  Ry for total energy and  $2.0 \times 10^{-3}$  Ry for maximum force, and 0.005 Ry smearing width to deal with

the presence of the Fermi surface (Malica and Corso, 2020). To obtain a smooth density of states (DOS), the tetrahedron method was applied with a denser  $k$ -mesh of 2744  $k$ -points in irreducible wedge of the BZ in performing the reciprocal space integrations.

Based on the tensorial form of Hooks law, which describes the linear dependency of the stress component  $\sigma_i$  ( $i=1-6$ ) and the applied strain  $\varepsilon_j$  ( $j=1-6$ ) under a small deformation (Nielsen and Martin, 1983), we compute the elastic stiffness/constants of the crystal using the finite difference approach as implemented in the Thermo-pw code (Malica and Corso, 2020). The perturbation of the crystal by a small strain  $\varepsilon_j$  is related to the stress tensor  $\sigma_j$  which returns it to equilibrium, and is given by the expression:

$$\sigma_i = \sum_j^6 C_{ij} \cdot \varepsilon_j \quad (1)$$

By applying a set of  $3 \times 3$  strain tensors leading to variations in the magnitude of lattice constant, the crystal size along the direction  $xy$ ,  $yz$ ,  $xz$  planes, for the applied strain ( $\varepsilon_j$ ) of magnitude  $-0.0075$ ;  $-0.0025$ ;  $+0.0025$ ; and  $+0.0075$  respectively. In addition, the average of both the positive (cell stretching) and negative (cell compressing) strains yields the final stress value. This procedure offers a minimal uncertainty in error estimation for final stress values during deformation for improved overall accuracy.

Further, using the approximate scheme of Voigt-Reuss-Hill (Voigt 1910, 1928; Reuss 1929; Hill, 1952), the calculations of bulk modulus (B), and shear modulus (G) were performed from the obtained elastic constants ( $C_{11}$ ;  $C_{12}$ ;  $C_{44}$ ) using equation 1. The schemes of Voigt (1928) and Reuss (1929) indicate the upper and lower bounds for structural parameters. The final values averages as (Hill, 1952):

$$B = (B_V + B_R)/2; \quad G = (G_V + G_R)/2 \quad (2)$$

The upper and lower bounds relate the bulk and shear moduli, and the elastic constants according to the VRH scheme:

$$B_V = \frac{1}{3}C_{11} + \frac{2}{3}C_{12}; \quad B_R = \frac{1}{3S_{11} + 6S_{12}} \quad (3)$$

and

$$G_V = \frac{1}{5}(C_{11} - C_{12}) + \frac{3}{5}C_{44}; \quad G_R = \frac{4}{C_{11} - C_{12}} + \frac{3}{C_{44}} \quad (4)$$

where  $C_{ij}$  and  $S_{ij}$  are the respective the elastic constants and elastic compliances. This method, though computationally expensive, has been applauded for its high accuracy in determining temperature dependent elastic properties of crystals (Malica and Corso, 2020) relative to other formalism (Yao *et al.*, 2007). Using ELATE package (Gaillac *et al.*, 2016), a direct visualization of the 3D spherical plot, likewise the 2D projections on (xy), (xz) and (yz) planes were generated using the  $C_{ij}$  moduli matrix obtained. Optical spectra calculation of response functions to electromagnetic waves was performed to estimate the photon-dependence complex dielectric function  $\varepsilon(\omega)$  given in the form (Ambrosch-Draxl and Sofo, 2018):

$$\varepsilon(\omega) = \varepsilon_1(\omega) + i\varepsilon_2(\omega) \quad (5)$$

where  $\varepsilon_2(\omega)$  and  $\varepsilon_1(\omega)$  are the imaginary and real frequency-dependent parts of dielectric function. Moreover, the imaginary part of the dielectric function  $\varepsilon_2(\omega)$ , is straightly linked to the band structure of materials and related absorptive treatment. The real part of dielectric function  $\varepsilon_1(\omega)$  is an extraction from the  $\varepsilon_2(\omega)$  using Kramers-Kronig (K-K) formalism; and it describes the electronic polarizability of materials using the expression below:

$$\varepsilon_2(\omega) = \frac{1}{\pi} \left[ \frac{\hbar e}{m\omega} \right]^2 \sum_{c,v} \int dk \langle c_k | P^\alpha | v_k \rangle \langle v_k | P^\beta | c_k \rangle \times \delta(\varepsilon_c^k - \varepsilon_v^k - \omega) \quad (6)$$

where c and v denote conduction and valence bands in basis sets and energies in the Kronecker

delta, and  $e, \omega, P$  denotes the electric charge, light frequency and momentum operator in  $\alpha$  and  $\beta$  directions. The real part obtained using K-K formalism is

$$\varepsilon_1(\omega) = \delta_{\alpha\beta} + \frac{2}{\pi} P \int_0^\infty d\omega' \frac{\omega' \text{Im} \varepsilon_2(\omega')}{(\omega')^2 - \omega^2} \quad (7)$$

Other calculated optoelectronic properties herein are the electron energy loss spectra  $L(\omega)$ , refractive index  $n(\omega)$ , extinction coefficient  $k(\omega)$ , and reflectivity  $R(\omega)$ , expressed as follows:

$$\left. \begin{aligned} L(\omega) &= \text{Im} \left[ \frac{-1}{\varepsilon(\omega)} \right] = \frac{\varepsilon_2(\omega)}{\varepsilon_1^2(\omega) + \varepsilon_2^2(\omega)} \\ n(\omega) &= \sqrt{\frac{|\varepsilon(\omega)| + \varepsilon_1(\omega)}{2}} \\ k(\omega) &= \sqrt{\frac{|\varepsilon(\omega)| - \varepsilon_1(\omega)}{2}} \\ R(\omega) &= \frac{(n-1)^2 + k^2}{(n+1)^2 + k^2} \end{aligned} \right\} \quad (8)$$

### 3.0 Results and Discussion

#### 3.1 Structural optimization and electronic properties

It is generally conspicuous that standard DFT-GGA calculations usually enhance geometrical structure as well as its relative stability in good agreement with experimental data. Semiconducting AlAs, is a B3-phase geometrical structure of the tetrahedral III-V arsenide composition with atomic configurations Al:  $[Ne] 3s^2 3p^1$  and As:  $[Ar] 3d^{10} 4s^2 4p^3$ . The coordination geometry of the B3 structure has Wyckoff positions of 4a and 4d within the site symmetry of subgroup  $F\bar{4}3m$ . The Bravais lattice of the B3 compound being face-centered cubic (FCC) crystal structure consists of two atoms per primitive unit-cell at  $T_1 = (0, 0, 0)$  and  $T_2 = (a_0/4)(1, 1, 1)$  with  $a_0$  being the lattice constant. In the optimized structure of AlAs B3-phase shown in Figure 2, the As-atom is tetrahedrally coordinated to four Al-atoms (wherein one atom is positioned at the edge and three others at their respective phases) as depicted in Figure 2(a).

To effectively reproduce the experimental lattice constant, the GGA approximation is adopted to obtain the lattice constant ( $a_0$ ) by fitting the energy-volume data to Birch–Munarghan equation of state (EOS) expressed as (Birch 1978):

$$E(V) = E_0 + \frac{9V_0B_0}{16} \left\{ \left[ \left( \frac{V_0}{V} \right)^{2/3} - 1 \right]^3 B' + \left[ \left( \frac{V_0}{V} \right)^{2/3} - 1 \right]^2 \left[ 6 - 4 \left( \frac{V_0}{V} \right)^{2/3} \right] \right\} \quad (9)$$

where  $V_0$  and  $V$  denote initial and deformed volume,  $B_0$  the bulk modulus and  $B'$  is a derivative of the bulk modulus at zero pressure. Shown in Figure 1 are the calculated and fitted energy-to-volume plots of our optimized data to obtain useful material properties. The properties obtained are displayed in Table 1, and comparisons with other theories and experimental values are depicted. The values of our lattice constant  $a_0$ , equilibrium volume  $V_0$  and bulk modulus  $B_0$  reveal consistency in our

calculations with experiments and theoretical data from reported literature. For instance, the calculated value of  $a_0 = 5.6756 \text{ \AA}$  (GGA) in our work is found to be in fair agreement with earlier reported value ( $a_0 = 5.660 \text{ \AA}$ ) by Greene *et al.* (1994) and ( $a_0 = 5.679 \text{ \AA}$ ) by Salmi *et al.* (2020). The accuracy of our structural optimization is again seen in the obtained value of Al-As bond-length of  $2.4576 \text{ \AA}$  (see Table 1) which is in accordance with reported values by Li *et al.* (2012). We also recorded Al-As-Al bond-angle of  $109.47^\circ$  in this study. Our DFT-GGA value of  $a_0$  overestimates experimental lattice constant (Greene *et al.*, 1994) by  $\approx 0.3 \%$  and unit-cell volume by  $0.9 \%$  but in accord with theory (Mugica *et al.*, 1999). The slight variation in our reported values is consistent with established facts from theories that DFT-GGA overestimates lattice constants and underestimates the band gaps.

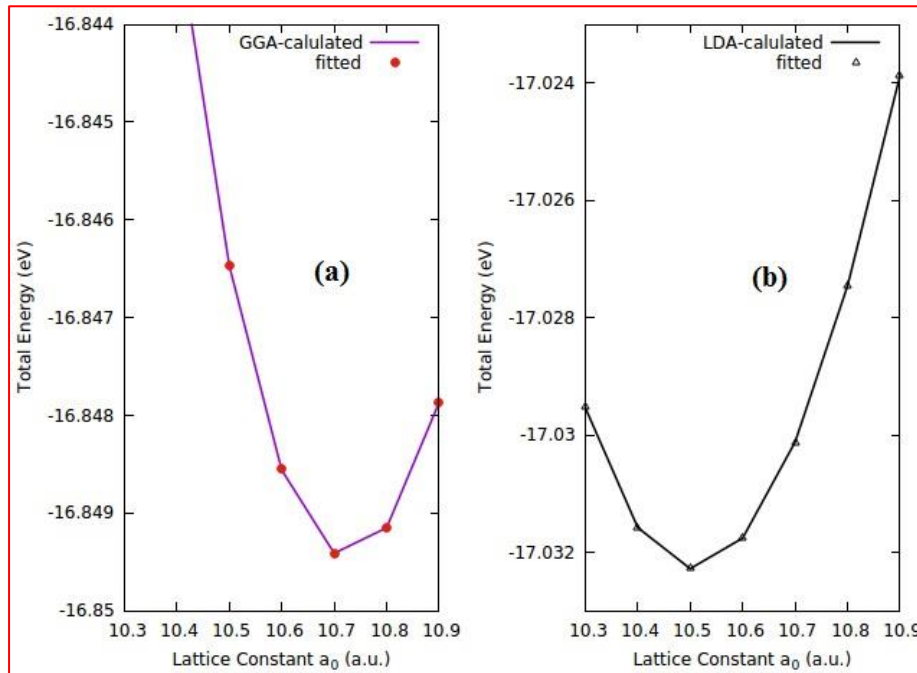


**Figure 1:** Dependence of lattice constant on total energy of AlAs from (a)-generalized gradient approximation (GGA) and (b)-local density approximation (LDA)

Figure 3((a) – (c)) presents the electronic band structure, density of state (DOS) and partial density of state (PDOS) of the optimized structural parameters. In Figure 3(a), a semiconducting behavior is revealed as the bands from the highest-occupied-molecular-orbitals (HOMO) and the lowest-unoccupied-molecular-orbitals (LUMO) within the Fermi-level do not overlap. As displayed in the figure, the HOMO divides into two distinct groups, showing lower and the upper groups occupying energy ranges of  $-12.1974$  to  $-10.1107$  eV, and  $-5.8004$  to  $-0.3615$  eV, respectively, with a HOMO bandwidth of  $7.0516$  eV. The HOMO-LUMO indirect band-gap energy at the  $\Gamma \rightarrow X$  symmetry points is  $1.45$  eV, which is further confirmed in the DOS plot of Figure 3(b). At the  $\Gamma$  symmetry point, a possible direct transition is observed. In general, the LUMO-HOMO transition lies at  $X \rightarrow \Gamma$  though, but at the  $\Gamma$ -point, the uppermost HOMO is made up of As (2p) and Al (1s) degenerate states resulting from the strong hybridization between As (p) and Al (s) states and small contributions from Al (2p) and localized d-states (see Figure 3c). Hence, the transition from the HOMO at  $\Gamma$  symmetry point originates from a degenerate non-dispersive HOMO region to the LUMO region. This trend is also reflected in our phonon frequency curve reported herein. Consequently, the lowest-unoccupied-molecular-orbital (LUMO), just above the Fermi level at X symmetry point is preponderated by the hybridization of delocalized As (3d) with Al (1s) and As (1s) states and minor contribution from As (2p) states to form single band.

Table 2 shows the directions at high symmetries in the Brillouin zone in relation to the energy transitions in the electronic band structure. Obviously, our reported indirect band gap is found at  $\Gamma \rightarrow X$ . Consequently, the energy transitions at  $\Gamma \rightarrow \Gamma$ ,  $X \rightarrow X$ ,  $W \rightarrow W$ ,  $K \rightarrow K$ ,  $\Gamma \rightarrow \Gamma$ ,

$L \rightarrow L$ ,  $U \rightarrow U$  are direct band energy at symmetry points  $\Gamma$ , X, W, K, L and U respectively. In Figure 3(c), the analysis of the partial density of states (PDOS) further establishes the modification around the electronic structure due to the projections of cation and anion orbitals. The hybridization of As (3d) and Al (1s) states plays a royal role in the formation of AlAs band gap.

### 3.2 Elastic constants and mechanical properties

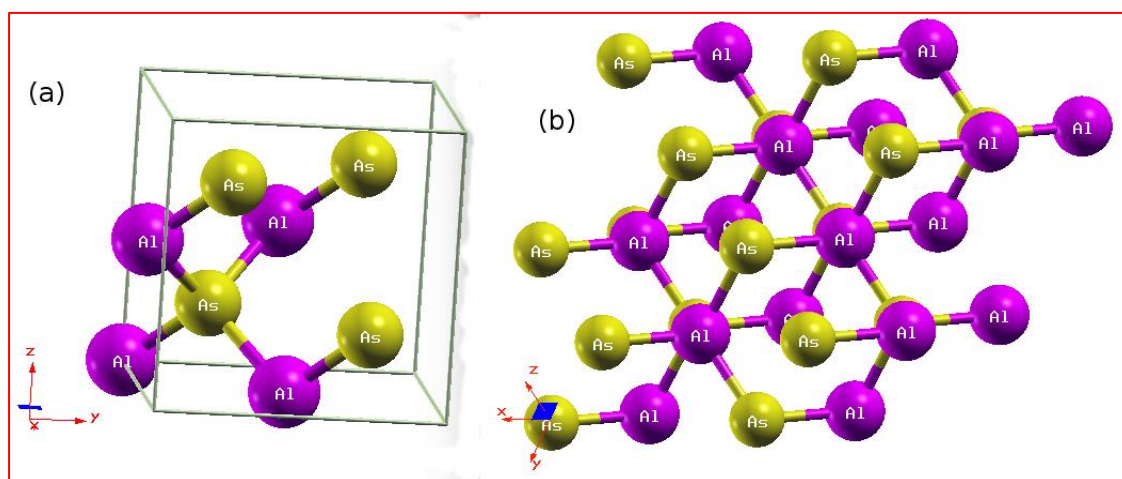
Among these review, calculation of elastic constants played very crucial role as many mechanically related parameters and properties rely on the elastic moduli. Cubical structural phases are known for having three independent  $C_{ij}$ . Potentially, the mechanical stability for cubical structures relies on Born and Huang's stability conditions (Born et al. 1955):

$$C_{11} - C_{12} > 0, C_{12} < B < C_{11}, C_{11} + 2C_{12} > 0, C_{11} > 0, C_{44} > 0$$

For cubic crystals, the three-independent elastic constants  $C_{11}$ ,  $C_{12}$ , and  $C_{44}$  (see Table 3) obtained in this work are in accord with, and hold true for the stability criterion of (Born *et al.*, 1955). Table 3 listed the calculated elastic constants  $C_{ij}$  and compliance matrices constants  $S_{ij}$  of AlAs with other moduli and reported data. Our calculated elastic constants are consistent with reported literature (Cui *et al.*, 2012), indicating reliability on both the adopted computational method and parameters. Also, the value of  $C_{11}$  is higher than  $C_{44}$  and  $C_{12}$  (transversal expansion), showing that the AlAs compound is hard to compress along [100] directions. Using the obtained results of our elastic moduli, and adopting Hill's approximation scheme (Hill, 1952), we calculated mechanical parameters like bulk modulus (B) and shear modulus (G) as applied in (Eq. (2), (3), and (4)).

**Table 1:** The lattice constant  $a_0$  (Å), bulk modulus  $B_0$  (GPa), first-pressure derivative  $B'$ , band gap  $E_g$  (eV), equilibrium volume  $V_0$  (Å<sup>3</sup>), Al-As and Al-Al bond-lengths (Å) for B3-AIAs

$a_0$ (Å)	$B_0$	$B'$	$E_g$ (eV)	$V_0$ (Å) <sup>3</sup>	Al-As $B_L$ (Å)	Al-Al $B_L$ (Å)	Method	References
5.676	67.500	3.970	1.450	45.710	2.475	4.041	GGA-PBE	This work
5.559	75.600	4.310	1.340	42.960	2.429	3.966	LDA	
5.660	74 ± 4	5.0 ± 1	-	-	-	-	Experiment	Green <i>et al.</i> , 1994
5.759	64.500	3.880	-	-	-	-	GGA-FP-LMTO	Wang <i>et al.</i> , 2009
5.641	74.100	-	-	-	-	-	LDA	Froyen <i>et al.</i> , 1983
5.650	75.850	4.820	1.330	-	-	-	LDA	Gupta <i>et al.</i> , 2009
5.640	-	-	1.600	-	-	-	GGA-PBE	Li <i>et al.</i> , 2012
-	75.000	4.300	-	44.520	-	-	LDA	Mujica <i>et al.</i> , 1995
5.720	74.000	4.601	1.850	-	-	-	LCAO	Munjal <i>et al.</i> , 2012
5.679	72.073	4.272	-	-	-	-	WC-GGA	Salmi <i>et al.</i> , 2020
5.634	75.543	4.555	2.259	-	-	-	LDA	Sansabilla <i>et al.</i> , 2023
5.733	71.855	4.383	-	-	-	-	GGA-PBE	
5.679	71.856	4.383	-	-	-	-	GGA-PBESOL	
5.640	76.410	4.160	-	-	-	-	LDA	Srivastava <i>et al.</i> 2011
5.720	-	-	-	-	-	-	GGA-PBE	
5.770	-	-	-	-	-	-	GGA-rev-PBE	
-	-	-	-	-	2.660	-	GGA	Guo <i>et al.</i> , 2008
5.670	75.200	4.370	-	-	-	-	GGA-PBE	Cui <i>et al.</i> , 2012
5.675	-	-	-	-	-	-	GGA-PBE	Zhang <i>et al.</i> , 2018
5.678	71.000	3.260	-	-	-	-	Pseudo-Potential	Zhang and Cohen 1987
5.660	82.000	4.182	1.950	-	-	-	FP-LMTO	Sheeba and Louis 2013
5.614	74.700	4.182	2.048	-	-	-	LDA	Wang and Ye., 2002

**Figure 2:** (a) Optimized unit-cell of zinc-blende AlAs. (b) 2x2x1 Supercell crystal structure of AlAs showing the various bonds. The purple (Solid) atoms represent the Al-atom while the yellow atoms represent

As-atom.

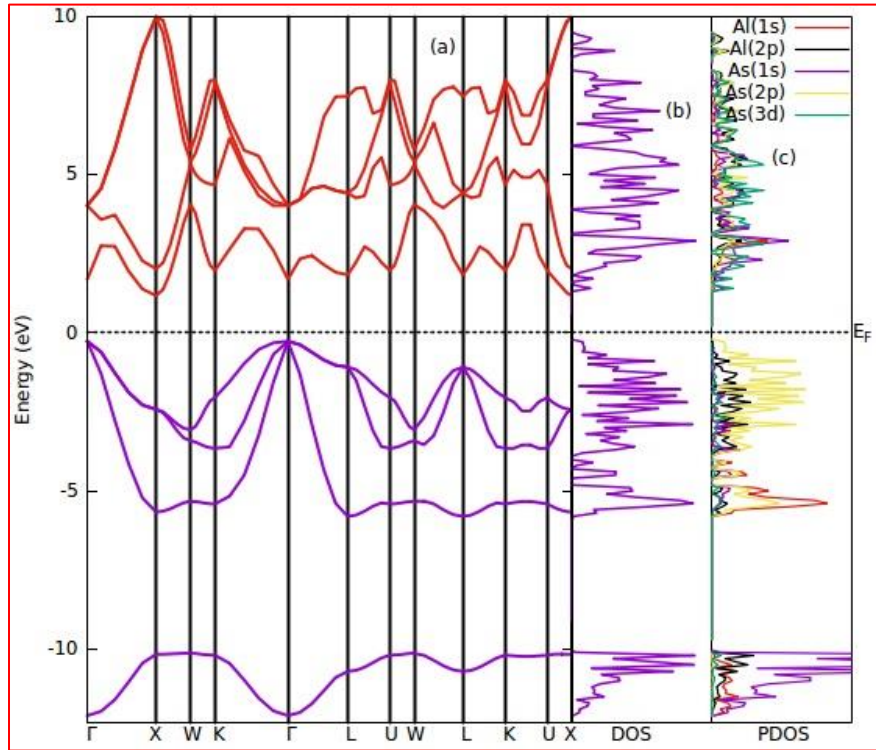


**Figure 3:** (a) Band structure of AlAs B3-phase. (The top of the HOMO is set to zero by subtracting the Fermi-energy  $E_F$ ), (b) density of state (DOS), (c) projected-DOS

**Table 2:** Energy transitions relating to high symmetry directions

Indirect energy transitions		Direct energy transitions	
$\Gamma \rightarrow X$	1.4449 (eV)	$\Gamma \rightarrow \Gamma$	1.9554 (eV)
$X \rightarrow W$	6.4701 (eV)	$X \rightarrow X$	3.5948 (eV)
$W \rightarrow K$	5.0327 (eV)	$W \rightarrow W$	7.1144 (eV)
$K \rightarrow \Gamma$	3.3738 (eV)	$K \rightarrow K$	4.0201 (eV)
$\Gamma \rightarrow L$	2.0989 (eV)	$L \rightarrow L$	2.9142 (eV)
$L \rightarrow U$	3.0528 (eV)	$U \rightarrow U$	4.0201 (eV)
$U \rightarrow W$	6.1018 (eV)		
$W \rightarrow L$	4.8941 (eV)		
$L \rightarrow K$	3.0528 (eV)		
$K \rightarrow U$	4.0201 (eV)		
$U \rightarrow X$	3.2265 (eV)		

From the estimated values of both B and G, we calculated mechanical properties like Young's modulus (E), Poisson's ratio ( $\nu$ ), and Vicker hardness ( $H_V$ ) given by Eqs. 10 and 11 respectively as Laref and Laref (2012) and Joshi *et al.* (2019) proposed:

$$E = 9BG/(3B + G); \quad \nu = [(3B/2G) - 1]/[(3B/G) + 1] \quad (10)$$

$$H_V = 0.92G^{0.708}(G/B)^{1.137} \quad (11)$$

$$A = 2C_{44}/(C_{11} - C_{12}) \quad (12)$$

$$A^U = (5G_V/G_R) + (B_V/B_R) - 6 \quad (13)$$

Also reported are calculated mechanical characteristics like Pugh's ratio ( $B/G$ ), Cauchy pressure ( $C_P$ ), Zener anisotropy factor ( $A$ ), universal anisotropy index ( $A^U$ ), etc. as given in Table 4. Succinctly, the bulk-modulus of Table 1 recorded from EOS and that of Table 4 obtained from elastic stiffness calculations are consistent, indicating resistance to volume-change due to strain. In general, materials Poisson's ratio value falls within the range  $0.25 < \nu < 0.5$  (Greaves *et al.*, 2011). However, a value of  $\nu < 0.3$  is an indication of a material's brittleness, while values of  $\nu > 0.3$  reveal ductile characteristics. According to Table 4, our obtained value for  $\nu$ , signatures a brittle character in AIs. Moreover, the lower the value of  $\nu$ , the greater its plasticity. Further, Pugh's ratio ( $B/G$ ) defines the ductility (or brittle) nature of a material from the critical-point  $B/G > 1.75$  (Pugh, 1954). Therefore, in classifying a material, it was found that, brittleness  $< 1.75 <$  ductility. Similarly, atomic bonding character of a compound likewise its ductile (or brittle) nature is also describe by the expression ( $C_P = C_{12} - C_{44}$ ) known as Cauchy pressure (Pettifor, 1992). A negative value of  $C_P$  is an indicator of a covalent bond (or brittleness) in a material, which correspond to a low Pugh's ratio ( $B/G < 1.75$ ) value. Similarly, a positive value of  $C_P$  is an indication of a metallic bond (or ductility), and correspond to a high Pugh's ratio ( $B/G > 1.75$ ) value. Thus, the recorded value of  $C_P$ , which of course is negative in the current study, confirms the conditions described by Poisson's and Pugh as expectable. Figures 4–7, show the calculated distribution in 2D-projections and 3D representations of the linear compressibility, Young's modulus, shear modulus and Poisson's ratio.

The Zener anisotropy factor ( $A$ ) and universal anisotropy index ( $A^U$ ), depict a materials behavior as isotropy (or anisotropy). If either  $A$

equals 1 (one) or  $A^U$  equals 0 (zero), then isotropy is exhibited in the compound, otherwise anisotropy is reflected for other cases. Using Eqs. 12 and 13, the calculated values are depicted in Table 4. The estimations from both approaches suggest anisotropy for AIs. Alternatively, the directionally dependent plots of Young and shear (rigidity) moduli, and Poisson's ratio are visually a way of showing Zener anisotropy. The implications of the elastic moduli  $C_{ij}$  to anisotropy in the B3-AIs structure as illustrated in Figures 4 – 7 are visible. The pronounced anisotropy is clearly visible in the three-dimensional distribution of the Poisson's ratio, Young and Shear moduli in Figures 5, 6, and 7 herein. By comparing the moduli distributions, it is obvious that the Young's and rigidity moduli are largest in the  $\langle 111 \rangle$ -directions, whereas the Poisson's ratio is greatest along the  $\langle 100 \rangle$  cubical axes. This generic behavior is found in a similar structure (Wu *et al.*, 2019), and reveals a direct consequence of the requirement  $A > 1$ . For anisotropic properties, the different responses to stress (or strain) in different directions is particularly crucial in applications where mechanical stress is required either directly or due to thermal expansion and contraction. Additionally, the melting temperature ( $T_m$ ) of the tetrahedrally coordinated AIs structure is defined by Wu *et al.* (2019):

$$T_m = \left[ 553 + \left( \frac{5.911}{GPa} \right) C_{11} \right] K \pm 300K \quad (14)$$

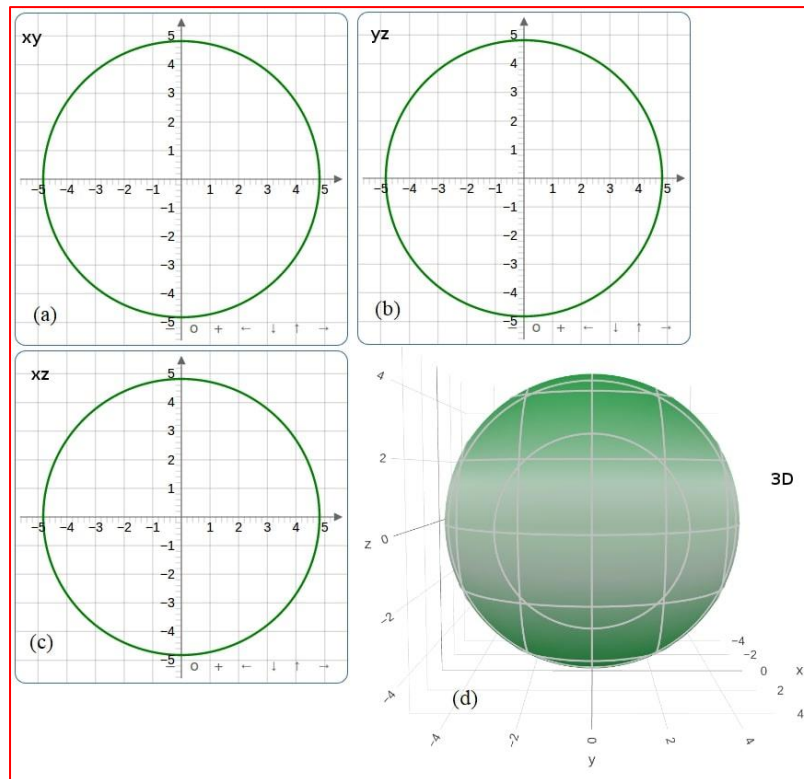
The  $T_m$  value shows that the resistance of the compound to temperature is low, which reveals the non-retention of crystal structure in the ground-state at high temperature.

**Table 3:** Elastic constants  $C_{ij}$ 's (in GPa), compliance matrices  $S_{ij}$ 's (1/Mbar), bulk and shear moduli (in GPa) representing the Voigt and the Reuss schemes

Model	$C_{11}$	$C_{12}$	$C_{44}$	$S_{11}$	$S_{12}$	$S_{44}$	$B_V$	$B_R$	$G_V$	$G_R$
<b>Present LDA work</b>	113.541	56.497	57.993	0.8807	-1.7700	1.7243	75.512	75.512	46.205	41.933
Cui <i>et al.</i> 2012										
<b>GGA</b>	114.78	53.56	60.12	-	-	-	-	-	-	-
Xing-xiu <i>et al.</i> , 2013										
<b>GGA</b>	119.2	54.8	60.4	-	-	-	-	-	-	-
Chetty <i>et al.</i> , 1989										
<b>GGA</b>	116.0	55.0	57.0	-	-	-	-	-	-	-

**Table 4:** Elastic moduli (in GPa) for B, G, E,  $\nu$ , B/G,  $C_P$ ,  $H_V$ , A, and  $A^U$ 

Model	B	G	E	$\nu$	B/G	$C_P$	$H_V$	A	$A^U$
<b>Present LDA work</b>	75.512	43.619	109.729	0.259	1.731	-1.496	7.140	2.033	0.630
<b>GGA</b>	69.121	41.287	103.295	0.251	1.674	-3.609	7.134	2.004	0.604

**Figure 4:** Calculated distribution in 2D-projections ((a) – (c)) and 3D representation (d) of linear compressibility

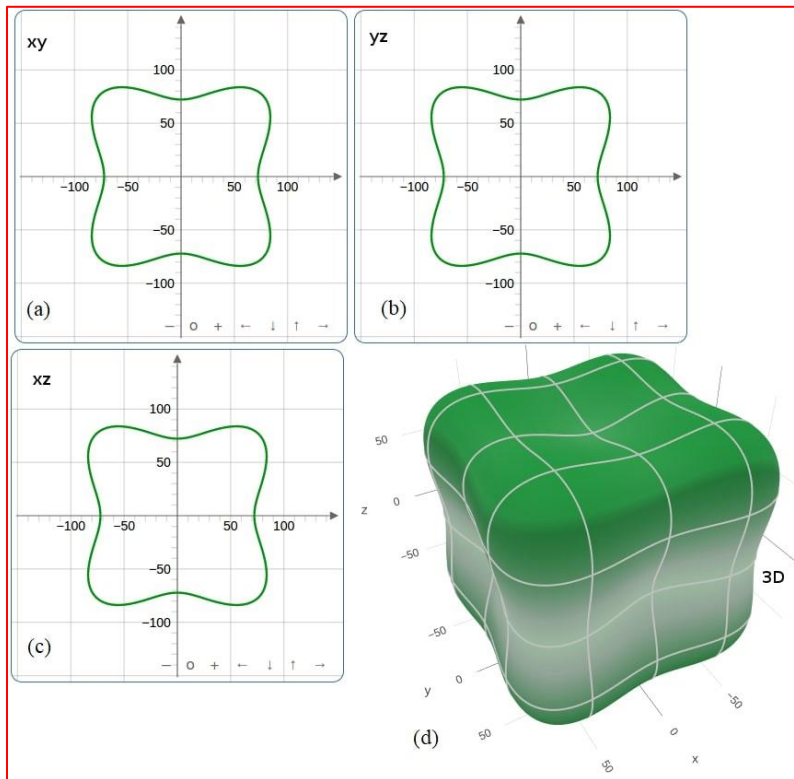


**Figure 5:** Calculated distribution in 2D-projections ((a) – (c)) and 3D representation (d) of Young's modulus

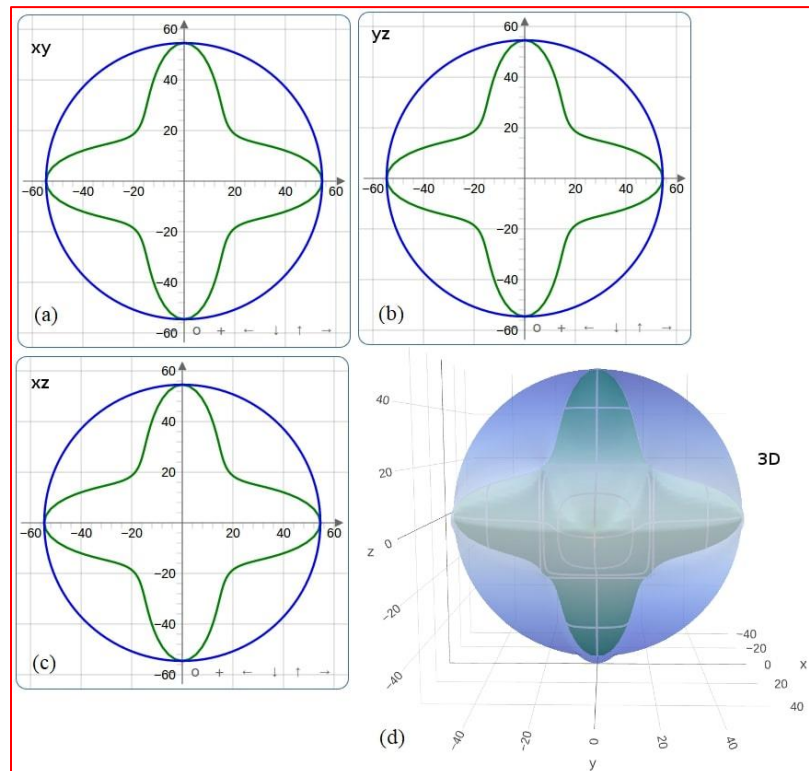


**Figure 6:** Calculated distribution in 2D-projections ((a) – (c)) and 3D representation (d) of Shear modulus

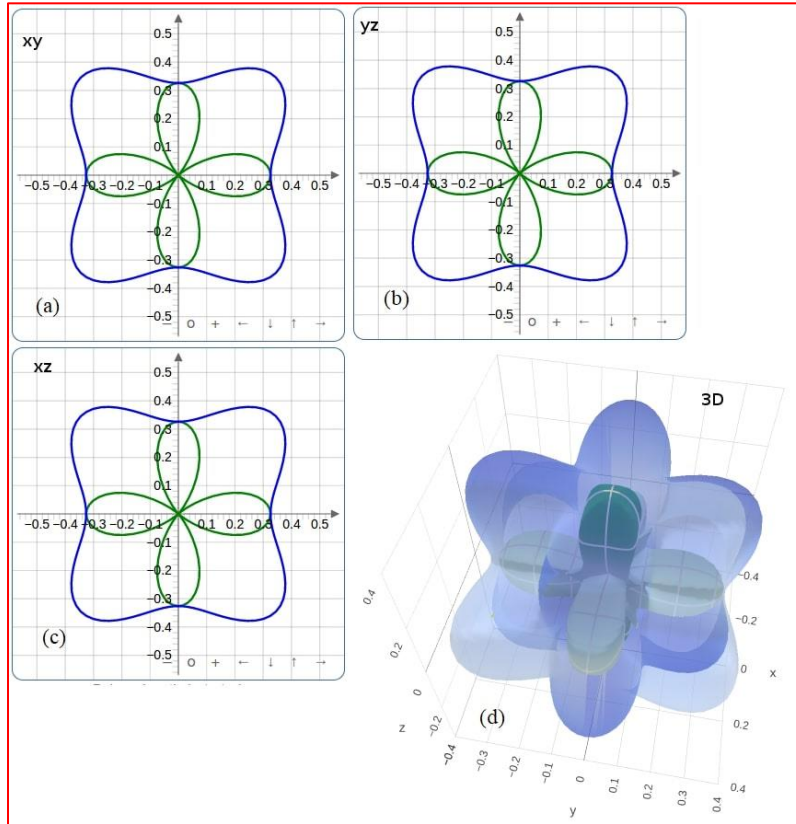


**Figure 7:** Calculated distribution in 2D-projections ((a) – (c)) and 3D representation (d) of Poisson's ratio

### 3.3 Thermodynamic properties

Thermodynamics studies are necessary to acquire corresponding properties as functions of temperature and pressure in terms of the quasi-harmonic Debye model, and have been successfully applied to estimate the thermodynamics properties of various materials. This procedure only needs energy-volume data to compute the Debye temperature, thermal expansion, heat capacity, and Grüneisen parameters for the compound. We calculated the Debye temperature ( $\Theta_D$ ) of AIAs from the average sound velocity ( $v_m$ ) using the standard formalism along with other properties such as constant volume heat capacity ( $C_V$ ), entropy, vibrational mean energy, and vibrational free energy. The standard formula for estimating the Debye temperature (Table 5) is defined by Zheng *et al.* (2015) and He *et al.* (2018):

$$\theta_D = \frac{h}{k_B} \left[ \frac{3n}{4\pi} \left( \frac{N_A \rho}{M} \right) \right]^{1/3} \cdot v_m \quad (15)$$

where  $h$  is the Planck's constant,  $k_B$  is the Boltzmann's constant,  $n$  is the number of atoms per formula unit,  $N_A$ ,  $\bar{M}$  and  $\rho$  denote Avogadro's number, molar mass, and density respectively. The average sound velocity  $v_m$  (Table 5) is described by the following equations:

$$v_m = \left[ \frac{1}{3} \left( \frac{2}{v_T^3} + \frac{1}{v_L^3} \right) \right]^{-1/3} \quad (16)$$

$$\text{where } v_T = \sqrt{\frac{G}{\rho}} ; v_L = \sqrt{\frac{3B+4G}{3\rho}} \quad (17)$$

where  $v_T$  and  $v_L$  are the transverse and longitudinal elastic wave velocity. The obtained Debye frequency  $\omega_D$  at zero pressure is defined by Poirier (2000) as:

$$\omega_D = (6\pi^2 N_A)^{1/3} \cdot \left(\frac{\rho}{M}\right)^{1/3} \cdot v_m \quad (18)$$

where  $\bar{M}$  is the mean atomic mass. The Grüneisen elastic parameter ( $\gamma$ ) for polycrystalline solids can be calculated in terms of Poisson ratio ( $\nu$ ) or from the sound velocities (Wu et al., 2019):

$$\gamma = \frac{3}{2} \left( \frac{1+\nu}{2-3\nu} \right) = [(9v_L^2 - 12v_T^2)/(2v_L^2 + 4v_T^2)] \quad (19)$$

In spectroscopy,  $\gamma$  is used to describe acoustical properties linked with averages as well as single crystal elastic stiffness coefficients.

Nevertheless, the results of the thermodynamic quantities computed within the quasi-harmonic approximation for AlAs structure are depicted in Figure 8 (Wallace, 1972). In the results, the Debye vibrational energy (or internal energy)  $U$ , Debye vibrational free energy  $F$ , Debye heat capacity at constant volume  $C_V$  and Debye entropy [ $S = (U - F)/T$ ] obtained with DFT within the temperature range 0 – 800 K is discussed as follows. A sharp increase in values of  $C_V$  and  $S$  is observed at high temperatures, which eventually tends to a constant above 600 K. The  $C_V$  reflects the heat storage capacity of solid materials and provides reasonable insight into their vibrational properties (Boutahar *et al.*, 2023). We observe in Figure 8(c) that the isochoric  $C_V$  of the AlAs increases exponentially with temperature for  $T < 350$  K while higher temperature range approaches the Dulong-Petit limit, which is an indication that all phonon modes at higher temperature are sufficiently excited by thermal energy (Bioud *et al.*, 2017). At 500 K, the recorded  $C_V$  is found to be circa  $48.42 \text{ Jmol}^{-1}\text{K}^{-1}$ . From the plots, the vibrational energy  $U$  at  $7.36 \text{ KJmol}^{-1}$  maintained its constant value up to circa 70 K, and thereafter monotonically increased slowly at higher temperatures. The Free energy  $F$ , in likewise manners, decreases abruptly as temperature

increases. Qualitatively, these behaviors are found in other semiconducting materials like boron arsenide (BAs) semiconductor and cubic rock-salt scandium mono-phosphide (ScP) as reported by Boutahar *et al.* (2023). Lastly, we observe the dependence of vibrational entropy  $S$  of the B3-AlAs material on temperature ranging from 0 K to 800 K. From the Figure 8(d), we found that at about 37K,  $S$  increases monotonously with temperature  $T$ . At 600 K, the recorded value of  $S$  is  $84.7 \text{ JK}^{-1}\text{mol}^{-1}$ . The low values of  $C_V$  and  $S$  recorded in this study is associated to the calculated low Debye temperature value of 397.724 K found for AlAs (see Table 5).

### 3.4 Optical properties

The optical spectra of B3-AlAs with crystal space-group  $F\bar{4}3m$  and Pearson symbol  $cF8$  are calculated. The behavior of imaginary part of dielectric function with other derivatives are investigated by the independent-particle approximation (IPA) using expanded basis sets obtained from the summation within the inter-band transitions of both the valence and conduction energy bands depicted by Eq. (6). The optical behavior of the B3-AlAs is as presented in Figures 9 and 10 respectively. Both the real  $\epsilon_1(\omega)$  and imaginary  $\epsilon_2(\omega)$  parts of dielectric function  $\epsilon(\omega)$  illustrate the material responsiveness to electromagnetic waves (EMW) as well as direct transitions linking to the HOMO and LUMO states due to dipole selection rules. The dielectric constants  $\epsilon_2(\omega)$  and  $\epsilon_1(\omega)$  depicted in Figure 9 are in the photon energy range of (0 – 25) eV. At near zero energy, the recorded static dielectric constant  $\epsilon_1(0)$  is 18.789 at 0.146 eV. The maximum value  $\epsilon_1(\omega) = 43.525$  was obtained at 1.74 eV (712.594 nm). The  $\epsilon_1(\omega)$  spectrum in comparison exhibits a different behavior from the spectrum of  $\epsilon_2(\omega)$ , and shows a more significant result.

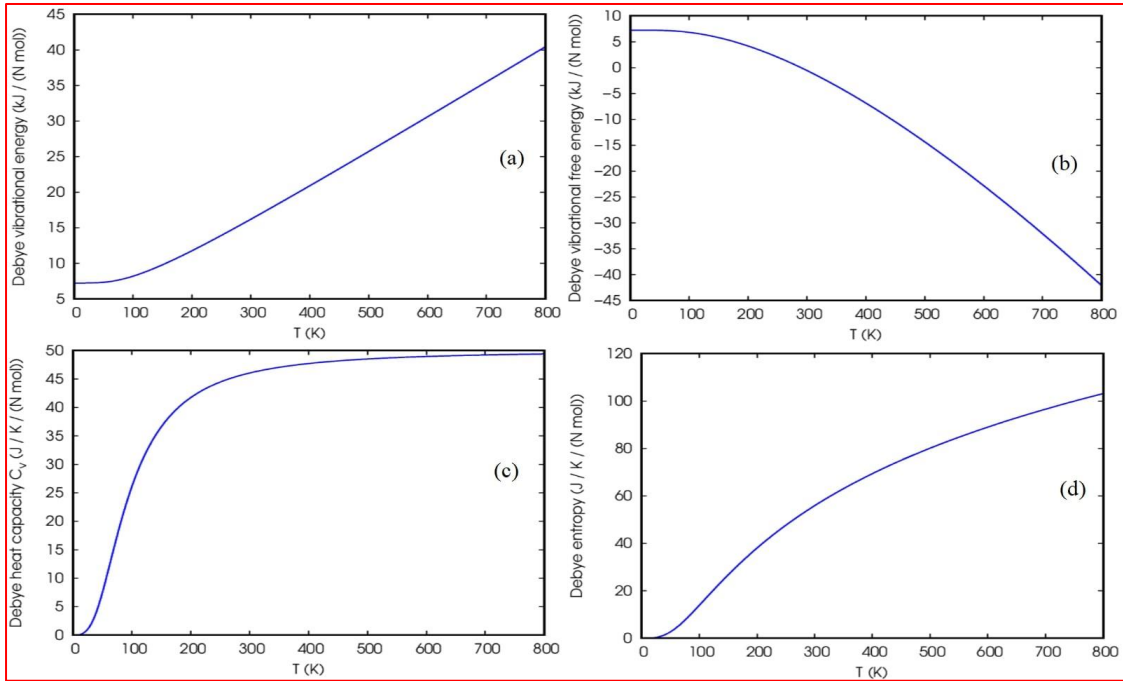


**Figure 8:** The figure depicts the temperature dependence of Debye vibrational mean energy (a), Debye vibrational free energy (b), Debye heat capacity (c) and Debye entropy (d) of B3-AIAs.

**Table 5:** Calculated compressional sound velocity ( $V_L$ ), shear sound velocity ( $V_T$ ), average sound velocity ( $V_m$ ), Debye frequency ( $\omega_D$ ), Grüneisen's parameter ( $\gamma$ ), average Debye sound velocity ( $V_{(D)}$ ), Debye temperature ( $\theta_{(D)}$ ) and melting temperature ( $T_m$ ) for B3-AIAs at ambient conditions

	GGA	LDA
$V_L$ (m/s)	5851.517	5908.921
$V_T$ (m/s)	3374.171	3371.754
$V_m$ (m/s)	3746.379	3747.094
$\omega_D$	$5.110 \times 10^{12}$	$5.111 \times 10^{12}$
$\gamma$	1.505	1.538
$V_{(D)}$ (m/s)	3711.024	3711.117
$\theta_{(D)}$ (K)	386.685	393.991
$T_m$ (K)	1456.190	1504.139

The negative data given by  $\epsilon_1(\omega)$  is an indication that electromagnetic wave has been reflected by the medium. This effect is potentially of great usefulness in radiation protection layers. Moreover, a negative dielectric constant ( $\epsilon_1(\omega) < 0$ ) depicts a metallic behavior whereas the positive values ( $\epsilon_1(\omega) > 0$ ) often signatures the dielectric nature of the material (Bashi *et al.*,

2021). As seen in Figure 9(a), the minimum value for  $\epsilon_1(\omega) = -20.62$  correspond to 3.02 eV (410.544 nm). The highest value of dielectric real part located at energy value of 1.739 eV is in the onset of infrared region of EMW, hence revealing the importance of AIAs to communication, cosmological and medical sectors. The other peaks are in decreasing steps

between the energy range of 2eV and 5.5 eV respectively. The three bottom peaks within these energy ranges belongs to the transitions from the three HOMO energy bands meeting together at  $\Gamma$ -point as seen in Figure 3.

The imaginary dielectric part  $\varepsilon_2(\omega)$  of B3-AIAs is shown also in Figure 9. The first peak is situated at 1.745 eV. Similarly, the majority and minority peaks situated between the energy at 2.805 to 5.05 eV are derived mostly from inter-band transitions of 2p-orbitals (in the HOMO region) to both 3d-orbital and 1s-orbitals (in the LUMO region). The spectral value of the first peak accords with the band-gap  $E_g$  value of the electronic structure (Figure 3). This means that the threshold energy of  $\varepsilon_2(\omega)$  in the spectrum is an electron transition between the HOMO and the LUMO. Furthermore, the  $\varepsilon_2(\omega)$  dielectric function links directly to the absorption coefficient of the system. The observed transition energies are mixed spectra of both ultraviolet and visible spectrum. Accordingly, Penn model proposes that the static dielectric constant and the obtained band-gap are inversely related by 
$$\left[ \varepsilon_1(0) \approx 1 + \left( \frac{\hbar\omega_p}{E_g} \right)^2 \right]$$
 (Amiri-Shookoh *et al.*, 2023). Noticeably, at higher energies above 15 eV, both the real and imaginary parts of the dielectric function huddled.

In Figure 10(a), the extinction coefficients  $k(\omega)$  just like in  $\varepsilon_1(\omega)$  and  $\varepsilon_2(\omega)$  parts of dielectric functions display four distinct corresponding peaks as clearly seen. From the calculated curve of  $k(\omega)$  for B3-AIAs, it can be deduced that the curve of extinction coefficient  $k(\omega)$  diligently follows the curve of imaginary part  $\varepsilon_2(\omega)$  of dielectric function. The deviations in the curves of  $k(\omega)$  and  $\varepsilon_2(\omega)$  can be tied to the limitations of the potential used which is yet unjustified owing to some absorption effects (Lavrentyev *et al.*, 2017). The high values of the  $k(\omega)$  are

observed at energies ranging from circa 1.877 eV to about 8.941 eV respectively. However, the first transition peak accords with those from the imaginary and real parts of dielectric functions.

Refractive index  $n(\omega)$  is another suitable candidate for describing the optoelectronic properties of materials. Being a dimensionless quantity,  $n(\omega)$  also tailors the characteristics of a beam propagated inside a medium. Figure 10(b) displays the calculated spectrum of  $n(\omega)$  as a function of photon energy. The eigenvalue of  $n(\omega)$  at zero energy can generally be estimated from the knowledge of  $\sqrt{\varepsilon_1(0)}$ . From Figure 10(b), the refractive index  $n(\omega)$  increases first to reach a maximum value, and thereafter decreases in the range 2.81 – 8.62 eV caused by electronic inter-band transitions. In the limits of the zero energy, the refractive index  $n(0)$  is 4.367, while its maximum value is 6.675 at 1.757 eV. After the next lower three peaks at 2.683, 3.866 and 5.323 eV, the  $n(\omega)$  then decreases and goes below unity from 9 eV with a change in the nature of optical properties from nonlinear to linear at circa 20 eV. In addition, this behavior below unity implies apparently that the velocity of incident radiation is thus greater than  $c$  (speed of light in vacuum).

Reflectivity  $R(\omega)$  variation with photon energy plot is shown in Figure 10(c). The spectral of  $R(\omega)$  is significantly and sequentially enhanced by the energy range starting from 1.757 eV and then sharply decreased at about 16.435 eV. Noticeably, the anisotropic nature of the reflectivity is over a considerable range of energy up to about 14 eV. From the reflectivity spectra, we observed that the intense peaks are situated at 3.08, 6.74, 10.26 and 13.86 eV respectively. Interestingly, the intensity of these peaks is approximately similar even at higher energies. Reflectivity coefficient at  $R(0)$  is 0.395 in magnitude. The obtained characteristic of  $R(\omega)$

is found in other B3-compounds like BeS (Elias, 2013).

Electron energy loss function (EELF) denoted by  $L(\omega)$  calculated is as shown in Figure 10(d). The spectral function  $L(\omega)$  plays a remarkable role in determining the surface and volume Plasmon energies. Obviously, at energies lower than the band-gap, no significant loss behaviors are recorded. In a crystal, it is possible to have several peaks known as Plasmon peaks in the spectrum of EELS. The Plasmon peaks explain the collective excitations of electron density within a crystal structure. The highest peak attained is the volume plasmon of the system corresponding to the Plasmon energy ( $\hbar\omega_p$ ). In Figure 9(c), the variation of EELF [ $L(\omega)$ ] with energy shows prominent peaks at expanded range of energy. From the Figure, there is pronounced incremental loss between the situated energies at 14 to 18 eV respectively. Additionally, a sharp decreasing peak shifted towards higher energies is observed. The estimated maximum loss of 9.9796 corresponds to the maximum intensity of the peak located at 17.24 eV (i.e. Volume Plasmon). Nevertheless, at energies lower than 14.0 eV moderated surface Plasmons with peaks less than unity are observed. This means that although the dielectric real part  $\epsilon_1(\omega)$  changes sign at the interface, the coherent delocalization of the electronic oscillations at the interface remains minimal due to the semiconducting nature of AlAs B3-phase.

### 3.5 Dynamical properties

**Phonon dispersion and stability:** To reveal the vibrational stability of the III–V semiconducting AlAs B3-phase, a phonon dispersion curve, as shown in Figure 11, is computed with the phonon DOS respectively. The phonon curve along the Brillouin zone  $\Gamma \rightarrow X \rightarrow K \rightarrow \Gamma \rightarrow L \rightarrow W \rightarrow X$  is produced using the quasi-harmonic approximation (Wallace, 1972) within the

Phonopy code described by Matsumoto *et al.* (2011). The phonon-frequency curve displays the acoustic and optical modes, consisting six phonon modes. Of the six modes are three low-lying acoustic phonon modes while the optical phonon modes are the rest. The absence of soft (imaginary) phonon mode in the whole Brillouin zone (BZ) confirms dynamically the compound's stability to vibrations. We observed two degeneracies at  $\Gamma$ -point, one each at the optical and acoustic regions. In solid state physics, phonon study in materials is pertinent as it helps to fathom clearly the physical characteristics of materials in relation to electron–phonon interactions, electrical conductivities, thermal expansion coefficients, specific heat, etc. Due to translational symmetry,  $\omega_j(k + G) = \omega_j(k)$  (with vibration frequency dependent wave vector  $k$ ), only phonon frequencies of the first BZ along high symmetry points can be calculated as depicted in the phonon dispersion curves of Figure 11 for AlAs B3-phase. Our calculation agrees well with the work of Li *et al.* (2012).

The present calculations observe that at the  $\Gamma$ -points, the symmetry directions  $\Gamma \rightarrow X$  and  $\Gamma \rightarrow L$  reveal four dispersion modes with a split into six branches in the directions  $L \rightarrow X$  and  $\Gamma \rightarrow X$ . A careful inspection of the phonon dispersions (or frequencies) includes verifying the number of longitudinal acoustical (LA) and transverse acoustical (TA) modes, as well as the longitudinal optic (LO) and transverse optic (TO) modes at Brillouin boundary. By characterizing the direction of high symmetry, one can identify the exact splitting at any given modes. Within the optical branch, recognizing the transverse mode (or longitudinal mode) is arduous except via cation/anion mass ratio consideration of constituent atoms and related ionicity (Spitzer, 1967).

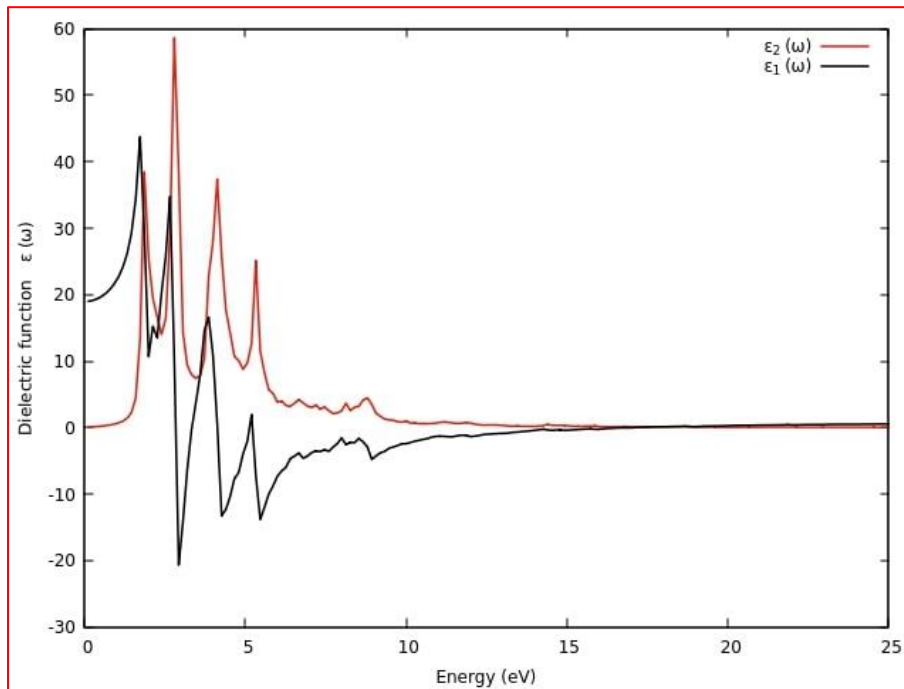


**Figure 9:** Dielectric constants dependence on photon energy for both the real and imaginary parts of AlAs B3-phase

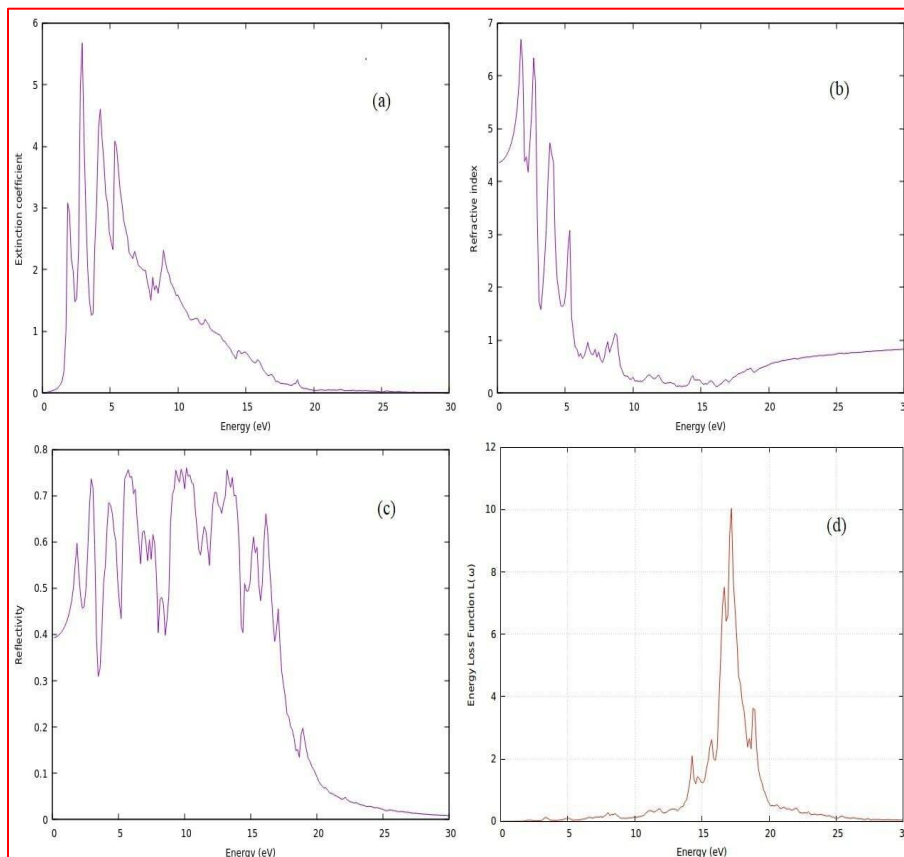


**Figure 10:** Extinction coefficient (a), Refractive index (b), Reflectivity (c), and Energy loss function (d) dependence on photon energy

However, in the acoustic domain such hassle is not experienced because the frequency of transversal branch is lower than that of longitudinal frequency with exceptions to zero frequency for both at BZ centres. Consequently, the reports by Spitzer (1967), Mitra (1963) and Adetunji *et al.* (2012) summarized these splits and four frequencies suffice usually ordered as: LO, TO, LA, and TA in order of decreasing frequency as recommended by the zone-edge values of the dispersion. The degenerate nature of the optical branch at the zone centres leads to the TO phonon modes having far higher energies than the LO mode at the zone boundary. Furthermore, low ionicity at the zone centre records a LO mode with higher frequency than the TO mode. Similarly, near zone boundary, the TO shows higher frequency relative to LO mode (Spitzer, 1967).

From the Figure 11, the dispersion of LO phonon mode in AIAs is distinct compared to other binary compounds of same family (Li *et al.*, 2012). Within this family, AIAs shows clear gap between the optic and acoustical frequency limits. This could be due to the small value of cation-to-anion mass ratio of 0.36 recorded for

AIAs, thereby leading to a much smaller phonon DOS peak. At  $\Gamma$  symmetry point, all the branches are clearly separated. Also, in the directions of  $\Gamma \rightarrow K$  and  $\Gamma \rightarrow L$  both the optical and acoustical branches split into transverse and longitudinal modes and with further mode splitting in directions of  $X \rightarrow K$ ,  $K \rightarrow \Gamma$ ,  $L \rightarrow W$ ,  $W \rightarrow X$  symmetries. Again, while the curve above  $350 \text{ cm}^{-1}$  is the LO mode, the one below  $350 \text{ cm}^{-1}$  is the TO mode. Similarly, the LA mode is the curve above  $200 \text{ cm}^{-1}$  while below  $100 \text{ cm}^{-1}$  is TA mode. Within the mode splitting regimes, the TA mode splits into two separate TA modes yielding  $2TA + 1LA$  (3 modes). In same vein, the splitting of TO mode is characterized by the optical regime where  $L \rightarrow W$  generates  $2TO + 1LO$  (3 modes). The equation by Lydane–Sachs–Teller (LST) relates the phonon frequencies  $\omega_{LO}$  and  $\omega_{TO}$  at  $\Gamma$ -point as  $[(\epsilon_0/\epsilon_\infty) = (\omega_{LO}^2/\omega_{TO}^2)]$ , where  $\epsilon_0$  and  $\epsilon_\infty$  denote static and high-frequency dielectric constants (Grosso and Parravicini, 2005, Li *et al.*, 2012). Table 6 presents the calculated values of our phonon frequencies ( $\text{cm}^{-1}$ ) for AIAs zinc-blende structure.

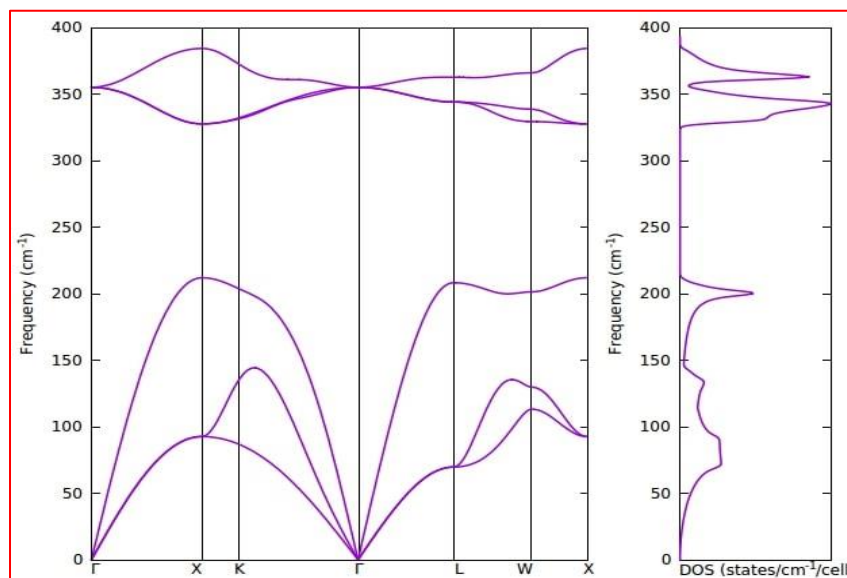


**Figure 11:** Phonon dispersion and phonon density of state (DOS) of B3-AIAs

**Table 6:** Calculated phonon frequencies (in  $cm^{-1}$ ) at high symmetry points  $\Gamma$ , X, K, L and W compared with other theoretical

Model AIs	$\Gamma$	X	K	L	W
TA	0.0	91.345	85.864/ 134.277	67.422	113.268/ 128.797
	0.0 <sup>(a)</sup>	107.4 <sup>(a)</sup>	-	217.9 <sup>(a)</sup>	135.3/ 140.8 <sup>(a)</sup>
LA	0.0	211.007	202.786	206.44	199.132
	0.0 <sup>(a)</sup>	220.7 <sup>(a)</sup>	-	220.7 <sup>(a)</sup>	199.7 <sup>(a)</sup>
TO	354.419	326.102	329.756	343.457	327.015/ 337.977
	363.9 <sup>(a)</sup>	334.3 <sup>(a)</sup>	-	352.4 <sup>(a)</sup>	338.5/ 339.5 <sup>(a)</sup>
LO	354.419	384.563	369.034	363.726	364.467
	399.1 <sup>(a)</sup>	391.3 <sup>(a)</sup>	-	369.1 <sup>(a)</sup>	344.5 <sup>(a)</sup>

<sup>(a)</sup>Li *et al.*, 2012

#### 4.0 Conclusions

A comprehensive investigation of B3-phase AIs from the structural, electronic, elastic, mechanical, thermodynamic, phonon-dispersion and optical properties has been carried-out based on first-principles calculations combining with the quasi-harmonic Debye model and frequency-dependent time-perturbation theory. Our calculated optimized lattice parameters of 5.594 (LDA) and 5.676 Å (GGA) are in close agreement with the experiment. The calculated structural properties are in good agreement with the available results. In the current study, B3-AIs has an indirect band gap of 1.45 eV (GGA) and 1.34 eV (LDA) as well as Al-As bond length of 2.4746 Å (GGA) and 2.4288 Å respectively. The structural and electronic parameters show a satisfactory agreement with available experimental values and theoretical results. Anisotropic analyses of the 3D-representations demonstrate that B3-AIs possesses high degree of anisotropy. The evaluated Debye temperature  $\theta_{(D)} = 397.724$  K reflects the feasibility of the material being brittle, while the Debye heat capacity  $C_V = 49.63$  J/(K.mol) reveals the Dulong-Petit limit. The Debye frequency ( $\omega_D$ ) and Grüneisen's parameter ( $\gamma$ ) of B3-AIs recorded are revealed for the first time. Furthermore, the optical calculations reveal additional properties like the extinction

coefficient, refractive index, reflectivity and electron energy loss function respectively. Lastly, we report calculations of phonon dispersion frequency for B3-AIs using the linear response method, making it possible to characterize the entire mode splitting into four dispersion modes. The non-imaginary phonon frequencies confirmed that the B3-AIs semiconducting state is satisfied with the structural stability. This work reveals the type of mode splitting presented in other reports.

#### Conflict of interest

The authors declare that they have no known competing financial interests that could have appeared to influence the work reported in this paper.

#### Acknowledgments

We thank the Abdus Salam International Centre for Theoretical Physics (ICTP), Trieste, Italy, for making available **EJDS** for journal repository.

#### References

- Adetunji, B.I., Adebambo, P.O., Adebayo, G.A., (2012). First principles studies of band structure and electronic properties of ZnSe. *J. Alloys Comp.*, 513: 294–299. <https://doi.org/10.1016/j.jallcom.2011.10.039>
- Ambrosch-Draxl, C., Sofo, J.O., (2006). Linear optical properties of solids within the full-

- potential linearized augmented planewave method. *Compt. Phys. Comm.*, 175(1): 1–14. <https://doi.org/10.1016/j.cpc.2006.03.005>
- Amiri-Shookoh, F., Aliabad, H.A.R., Tavakoli-Anbaran, H., (2023). Comparative DFT calculations on Bismuth-based compounds: new connection between optoelectronic properties and  $^{209}\text{Bi}$  and  $^{51}\text{V}$  NMR and EFG. *Indian J. Phys.*, 97(3): 797–807. <https://doi.org/10.1007/s12648-022-02458-1>
- Bashi, M., Asghar, H., Aliabad, R., (2021). Optoelectronic and thermoelectric properties of DMAP flexible compound for electronic devices by DFT. *Optical and Quantum Electronics*, 53: 1–12. <https://doi.org/10.1007/s11082-021-02853-8>
- Bioud, N., Kassali, K., Bouarissa, N., (2017). Thermodynamic Properties of Compressed CuX (X = Cl, Br) Compounds: Ab Initio Study. *J. Electron. Mater.* 46, 2521–2528. <https://doi.org/10.1007/s11664-017-5335-x>
- Birch, F., (1978). Finite strain isotherm and velocities for single-crystal and polycrystalline NaCl at high pressures and 300°K. *J. Geophys. Res.: Solid Earth*, 83: 1257–1268. <https://doi.org/10.1029/JB083-IB03P01257>
- Born, M., Huang, K., Lax, M., (1955). Dynamical theory of crystal lattices. *Am. J. Phys.*, 23(7): 474–474. <https://doi.org/10.1119/1.1934059>
- Boutahar, L., Benamrani, A., Rouabah, Z., Daoud, S., (2023).  $\text{Cu}_2\text{ZnSnS}_4$  Materials: THEORETICAL PREDICTION. *Sciendo*, 67: 160–170. <https://doi.org/10.2478/awutp-2023-0012>
- Cai, J., Chen, N., (2007). Theoretical study of pressure-induced phase transition in AlAs: From zinc-blende to NiAs structure. *Phys. Rev. B.*, 75. <https://doi.org/10.1103/PhysRevB.75.174116>
- Chetty, N., Muoz, A., Martin, R., (1989). First-principles calculation of the elastic constants of AlAs. *Phys. Rev. B, Condens. Matt.*, 40 (17): 11934 - 11936. <https://doi.org/10.1103/PhysRevB.40.11934>
- Cui, H., Lv, S., Ji, G., (2012). Structural and elastic properties of AlAs under pressure from first-principles calculations, *Adv. Mater. Res.* (Volumes 403-408), 84-87. <https://doi.org/10.4028/www.scientific.net/AMR.403-408.84>
- Ekong, S.A., Fuwape, I.A., Odo, E.A., (2014). Ab initio study of the electronic structure of silicon quantum dots. *J. Nig. Assoc. Math. Phys.*, 26: pp.177–186.
- Ekong, S.A., Oloye, M.T., Oyegoke, D.A., (2015). Ground-state energy calculation of helium atom using quantum Monte Carlo casino-code, *Adv. Phys. Theo. Applications*, Vol. 46, 1 - 6.
- Elias, B., (2013). Theoretical investigation of the structural, electronic, elastic and optical properties of zinc-blende BeS under high pressure. *Intl. J. Inn. Res. Sci., Engr. & Tech.*, 2 (9): 4193-4204.
- Froyen, S., Cohen, M.L., (1983). Structural properties of III-V zinc-blende semiconductors under pressure, *Phys. Rev. B*, 28(6), 3258–3265. <https://doi.org/10.1103/PhysRevB.28.3258>
- Gaillac, R., Pullumbi, P., Francois-Xavier, C., (2016). An open-source online application for analysis and visualization of elastic tensors. *J. Phys. Condens. Matt.*, 28: 275201. <https://doi.org/10.1088/0953-8984/28/27/275201>
- Giannozzi, P., Baroni, S., Bonini, N., Calandra,

- M., Car, R., Cavazzoni, C., Ceresoli, D., Chiarotti, G.L., Cococcioni, M., Dabo, I., Da-Corso, A., De-Gironcoli, S., Fabris, S., Fratesi, G., Gebauer, R., Gerstmann, U., Gougoussis, C., Kokalj, A., Lazzeri, M., Martin-Samos, L., Marzari, N., Mauri, F., Mazzarello, R., Paolini, S., Pasquarello, A., Paulatto, L., Sbraccia, C., Scandolo, S., Sclauzero, G., Seitsonen, A.P., Smogunov, A., Umari, P., Wentzcovitch, R.M., (2009). QUANTUM ESPRESSO: A modular and open-source software project for quantum simulations of materials. *J. Phys. Condens. Matt.*, 21. <https://doi.org/10.1088/0953-8984/21/39/395502>
- Goedecker, S., Teter, M., (1996). Separable dual-space Gaussian pseudopotentials. *Phys. Rev. B - Condens. Matter. Phys.*, 54: 1703–1710. <https://doi.org/10.1103/PhysRevB.54.1703>
- Greaves, G.N., Greer, A.L., Lakes, R.S., Rouxel, T., (2011). Poisson's ratio and modern materials. *Nat. Mater.*, 10: 823–837. <https://doi.org/10.1038/nmat3134>
- Greene, R.G., Luo, H., Li, T., Ruoff, A.L., (1994). Phase transformation of AlAs to NiAs structure at high pressure, *Phys. Rev. Lett.*, 72: 2045–2048. <https://doi.org/10.1103/PhysRevLett.72.2045>
- Grosso, G., Parravicini, G.P., (2014). Solid State Physics, 2<sup>nd</sup> Edition, Elsevier Ltd. Library of Congress Cataloging-in-Publication Data. ISBN: 978-0-12-385030-0
- Guo, L., (2011). Structural, energetic, and electronic properties of hydrogenated aluminum arsenide clusters. *J. Nanopart. Res.*, 13: 2029–2039. [DOI 10.1007/s11051-010-9957-7](https://doi.org/10.1007/s11051-010-9957-7)
- Gupta, D.C., Kulshrestha, S. (2009). Effect of high pressure on polymorphic phase transition and electronic structure of XAs (X = Al, Ga, In), *Phase Transitions*, Vol. 82, No. 12, 850–865. <https://doi.org/10.1080/01411590903326628>
- Hartwigsen, C., Goedecker, S., Hutter, J., (1998). Relativistic separable dual-space Gaussian pseudopotentials from H to RnC. *Phys. Rev. B*, 58: 3641–3662. <https://doi.org/10.1103/PhysRevB.58.3641>
- He, W., Huang, H., Liu, Z., Ma, X., (2018). First-principles calculations on elastic, magnetoelastic, and phonon properties of Ni<sub>2</sub>FeGa magnetic shape memory alloys. *Chine. Phys. B* 27, 016201. <https://doi.org/10.1088/16741056/27/1/016201>
- Hill, R., (1952). The Elastic Behaviour of a Crystalline Aggregate. *Proc. Phys. Soc., Section A* 65: 349. <https://doi.org/10.1088/0370-1298/65/5/307>
- Jappor, H.R., Saleh, Z.A., Abdulsattar, M.A. (2013). Electronic structure of aluminum arsenide nanocrystals Using Ab initio large unit cell method. *J. Babylon University/Pure and Applied Sciences*, Vol. (21), No. (7): 2464 - 2476.
- Jiang, M., Xiao, H., Peng, S., Qiao, L., Yang, G., Liu, Z., Zu, X., (2018). First-principles study of point defects in GaAs/AlAs superlattice: the phase stability and the effects on the band Structure and carrier mobility, *Nanos. Res. Lett.*, 13: 301. <https://doi.org/10.1186/s11671-018-2719-7>
- Jolayemi, O.R., Ekong, S.A., (2020). Electronic, structural, magnetic and mechanical properties of Mg<sub>1-x</sub>Sr<sub>x</sub>N rocksalt from first-principles. *Trans. Nig. Assoc. Math. Phys.*, 13, pp.39 – 44.
- Jolayemi, O.R., Ekong, S.A., Adetunji, B.I.,

- Iboh, U.A., (2019). First-principles study of half-metallic ferromagnetism in (1 1 1) surface of CsSe. *J. Nig. Assoc. Math. Phys.*, 51, pp.157–162
- Joshi, H., Rai, D.P., Hnamte, L., Laref, A., Thapa, R.K., (2019). A theoretical analysis of elastic and optical properties of half Heusler MCoSb (M = Ti, Zr and Hf). *Heliyon*: e01155. <https://doi.org/10.1016/j.heliyon.2019.e01155>
- Kimukin, I., Biyikli, N., Kartaloglu, T., Aytur, O., Ozbay, E., (2004). High-speed InSb photodetectors on GaAs for mid-IR applications. *IEEE J. Selected Topics in Quantum Electronics*, 10(4): 766-770. DOI: [10.1109/JSTQE.2004.833891](https://doi.org/10.1109/JSTQE.2004.833891)
- Kohn, W., Sham, L.J., (1965). Self-consistent equations including exchange and correlation effects, *Phys. Rev.* 140, p. A1133. <https://doi.org/10.1103/PhysRev.140.A1133>
- Laref, S., Laref, A., (2012). Thermal properties of BeX (X = S, Se and Te) compounds from ab initio quasi-harmonic method. *Compt. Mater. Sci.*, 51: 135–140. <https://doi.org/10.1016/j.commatsci.2011.07.016>
- Lavrentyev, A.A., Gabrelian, B.V., Vu, V.T., Ananchenko, L.N., Isaenko, L.I., Yelisseyev, A.P., Khyzhun, O.Y., (2017). Electronic structure and optical properties of noncentrosymmetric LiGaSe<sub>2</sub>: Experimental measurements and DFT band structure calculations. *Optic. Mater.*, 66: 149–159. <https://doi.org/10.1016/j.optmat.2017.01.049>
- Lebga, N., Daoud, S., Sun, X., Bioud, N., Latreche, A. (2018). Mechanical and thermophysical properties of cubic rock-salt AlN under high pressure. *J. Electron. Mater.* 47, 3430–3439. <https://doi.org/10.1007/s11664-018-6169-x>
- Li, X., Tao, X., Li, R., Chen, H., Ouyang, Y., Du, Y., (2012). Lattice dynamics properties of XAs (X=Al, Ga and In) with zinc-blende structure from first-principle calculations. *J. Phys. Chem. Sol.*, 73: 1034–1039. <https://doi.org/10.1016/j.jpcs.2012.03.010>
- Liu, G.C., Lu, Z.W., Klein, B.M., (1994). Pressure-induced phase transformations in AlAs: Comparison between *ab initio* theory and experiment, *Phys. Rev. B*, 51: 5678. <https://doi.org/10.1103/PhysRevB.51.5678>
- Malica, C., Corso, A.D., (2020). Quasi-harmonic temperature dependent elastic constants: applications to silicon, aluminum, and silver. *J. Phys. Condens. Matt.*, 32. <https://doi.org/10.1088/1361-648X/ab8426>
- Matsumoto, A., Koyama, Y., Togo, A., Choi, M., Tanaka, I., (2011). Electronic structures of dynamically stable As<sub>2</sub>O<sub>3</sub>, Sb<sub>2</sub>O<sub>3</sub>, and Bi<sub>2</sub>O<sub>3</sub> crystal polymorphs. *Phys. Rev. B - Condens. Matter. Mater. Phys.*, 83. <https://doi.org/10.1103/PhysRevB.83.214110>
- Mitra, S.S., (1963). Phonon Assignments in ZnSe and GaSb and Some Regularities in the Phonon Frequencies of Zincblende-Type Semiconductors. *Phys. Rev.* 132 (3): 986–991. <https://doi.org/10.1103/PhysRev.132.986>
- Monkhorst, H.J., Pack, J.D., (1976). Special points for Brillouin-zone integrations. *Phys. Rev. B* 13: 5188. <https://doi.org/10.1103/PhysRevB.13.5188>
- Mugica, A., Rodriguez-Hernandez, P., Radescu, S., Needs, R.J., Munoz, A., (1999). AlX (X = As, P, Sb) compounds under pressure, *Phys. Stat. Sol. (b)* 211, 39: 39–44. [https://doi.org/10.1002/\(SICI\)15213951\(199901\)211](https://doi.org/10.1002/(SICI)15213951(199901)211)

- Mujica, A., Rubio, A., Munoz, A., Needs, R.J., (2003). High-pressure phases of group-IV , III – V , and II – VI compounds. *Rev. Mod. Phys.*, 75: 863–912. <https://doi.org/10.1103/RevModPhys.75.863>
- Mujica, A., Rubio, A., Munoz, A., Needs, R.J., (1995). First-principles pseudopotential study of the phase stability of the III-V semiconductors GaAs and AlAs. *Phys. Rev. B*, 52 (12): 8881–8891. <https://doi.org/10.1103/PhysRevB.52.8881>
- Munjaj, N., Sharma, G., Vyas, V., Joshi, K.B., Sharma, B.K., (2012). Ab-initio study of structural and electronic properties of AlAs, *Philosophical Magazine*, 92, (24): 3101–3112. <http://dx.doi.org/10.1080/14786435-2012.685189>
- Nielsen, O.H., Martin, R.M., (1983). First-principles calculation of stress. *Phys. Rev. Lett.* 50: 697–700. <https://doi.org/10.1103/PhysRevLett.50.697>
- Perdew, J.P., Burke, K., Ernzerhof, M., (1996). Generalized Gradient Approximation Made Simple. *Phys. Rev. Lett.* 77: 3865. <https://doi.org/10.1103/PhysRevLett.77.3865>
- Pettifor, D.G., (1992). Theoretical predictions of structure and related properties of intermetallics. 8 (4): 345–349. <https://doi.org/10.1179/mst.1992.8.4.345>
- Poirier, J.-P., (2000). Introduction to Physics of the Earth's Interior. Second Edition. Published by the press Syndicate of the University of Cambridge, the Pitt building, trumpington street, Cambridge, United Kingdom. ISBN 0 521 66392 X
- Pugh, S.F., (1954). XCII . Relations between the elastic moduli and the plastic properties of polycrystalline pure metals, *Philoso. Mag. Seri. 7 & J. Sci.*, 45: 823–843. <https://doi.org/10.1080/14786440808520496>
- Reuss, A., (1929). Berechnung der Fließgrenze von Mischkristallen auf Grund der Plastizitätsbedingung für Einkristalle . *ZAMM - J. Appl. Math. & Mechan. / Zeitschrift für Angewandte Mathematik und Mechanik* 9: 49–58. <https://doi.org/10.1002/ZAMM.19290090104>
- Salmi, L., Meradji, H., Ghemid, S., Nemiri, O., Oumelaz, F., Khenata, R., Meradji, H., Ghemid, S., Nemiri, O., Oumelaz, F., Khenata, R., (2020). Phase stability, pressure-induced phase transition and electronic properties of AlX (X = P, As and Sb) compounds from first principle calculations. *Phase Transitions* 93(9):1–13. <https://doi.org/10.1080/01411594.2020.1795858>
- Sansabilla, B., Rachid, T., (2023). Structure, electronic properties of AlAs using first-principles calculations, Advanced Topics in Mechanics of Materials, Structures and Construction – AtoMech, Materials Research Forum LLC, *Mater. Res. Proc.*, 31, 204-211. <https://doi.org/10.21741/9781644902592-2>
- Shafei, L., Adhikari, P., Ching, W.-Y., (2021). DFT study of electronic structure and optical properties of Kaolinite, Muscovite, and Montmorillonite. *Crystals*, 11 (6): 618. <https://doi.org/10.3390/cryst11060618>
- Sheeba, V.B., Louis, C.N., (2013). Band structure, metallization and superconducting transition of group III-V semiconductors AlP and AlAs under high pressure, *Chem. Mater. Engr.*, 1(4): 132-140. [DOI:10.13189/cme.2013.010405](https://doi.org/10.13189/cme.2013.010405)

- Spitzer, W.G., (1967). Multiphonon Lattice Absorption. *Semiconductors and Semimetals*, 3, p.17-69. [https://doi.org/10.1016/S00808784\(08\)60314-2](https://doi.org/10.1016/S00808784(08)60314-2)
- Srivastava, A., Tyagi, N., Sharma, U.S., Singh, R.K., (2011). Pressure induced phase transformation and electronic properties of AlAs. *Mater. Chem. Phys.*, 125: 66–71. <https://doi.org/10.1016/j.matchemphys.2010.08.072>
- Varshney, D., Joshi, G., Kaurav, N., Singh, R.K. (2009). Structural phase transition (zincblende–rocksalt) and elastic properties in AlY (Y = N, P and As) compounds: Pressure-induced defects. *J. Phys. Chem. Solid.*, 70, pp.451–458
- Voigt, W., (1910). Lehrbuch der kristallphysik (mit ausschluß der kristalloptik). B.G. Teubner, Leipzig;Berlin.; Voigt, W., (1928). Lehrbuch de Kistallphysik.: 739.
- Vurgaftman, I., Meyer, J.R., Ram-Mohan, L.R., (2001). Band parameters for III–V compound semiconductors and their alloys. *J. Appl. Phys.* 89, 5815–5875. <https://doi.org/10.1063/1.1368156>
- Wallace, D.C., (1972). Thermodynamics of Crystals. Published by John Wiley & Sons, Inc. Printed in the United States of America. ISBN 0-471-91855-5
- Wang, H.Y., Xu-Sheng, L., Chang-Yun, L., Kuang-F.W., (2009). First-principles study of phase transition and structural properties of AlAs, *Mater. Chem. Phys.*, 117, 373–376, [doi:10.1016/j.Matchemphys.2009.06.006](https://doi.org/10.1016/j.Matchemphys.2009.06.006).
- Wang, S.Q., Ye, H.Q., (2002). A plane-wave pseudopotential study on III-V zinc-blende and wurtzite semiconductors under pressure. *J. Phys.: Condens. Matt.*, 14 (41), 9579–9587. [doi:10.1088/0953-8984/14/41/313](https://doi.org/10.1088/0953-8984/14/41/313).
- Wu, S.C., Fecher, G. H., Shahab, N. S., Felser, C., (2019). Elastic properties and stability of Heusler compounds: Cubic Co<sub>2</sub>YZ compounds with L2<sub>1</sub> structure. *J. Appl. Phys.*, 125. <https://doi.org/10.1063/1.5054398>
- Xing-xiu, L., Xiao-Ma, T., Hong-Mei, C., Yi-Fang, O., Yong, D., (2013). The pressure dependences of elastic and lattice dynamic properties of AlAs from ab initio calculations. *Chinese Phys. B* 22 026201. <https://doi.org/10.1088/16741056/22/2/026201>
- Yao, H., Ouyang, L., Ching, W.Y., (2007). Ab initio calculation of elastic constants of ceramic crystals. *J. Am. Ceram. Soc.*, 90: 3194–3204. <https://doi.org/10.1111/j.1551-2916.2007.01931.x>
- Zhang, S.B., Cohen, M.L., (1987). High-pressure phases of III-V zinc-blende semiconductors, *Phys. Rev. B*, Vol. 35, No. 14, 7604–7610. <https://doi.org/10.1103/PhysRevB.35.7604>
- Zhang, W., Changchun, C., Yanxing, S., Qingyang, F., Yintang, Y., (2018). Structural, mechanical, anisotropic, and thermal properties of AlAs in oC12 and hP6 phases under pressure, *Materials*, 11(5), 740. <https://doi.org/10.3390/ma11050740>
- Zheng, B., Zhang, M., Luo, H., (2015). Pressure effect on structural, elastic, and thermodynamic properties of tetragonal B<sub>4</sub>C<sub>4</sub>. *AIP ADVANCES* 5, 037123. <https://dx.doi.org/10.1063/1.4915257>